Photocatalysis
https://www.sciltp.com/journals/photocatalysis

Article

Photocatalytic Hydrogen Generation over Natural Sepiolite and Palygorskite

Patrik Kopčan [1,2], Alexandr Martaus [1] and Kamila Kočí [1,3,*]

[1] Institute of Environmental Technology, Center for Energy and Environmental Technology, VŠB-Technical University of Ostrava, 70800 Ostrava, Czech Republic
[2] Faculty of Materials Science and Technology, VŠB-Technical University of Ostrava, 70800 Ostrava, Czech Republic
[3] Department of Physics and Materials Engineering, Faculty of Technology, Tomáš Baťa University in Zlín, 76001 Zlín, Czech Republic
* Correspondence: kamila.koci@vsb.cz

How To Cite: Kopčan, P.; Martaus, A.; Kočí, K. Photocatalytic Hydrogen Generation over Natural Sepiolite and Palygorskite. *Photocatalysis* **2026**, *2*(1), 2. https://doi.org/10.53941/photocatalysis.2026.100002

Received: 21 January 2026
Revised: 20 February 2026
Accepted: 11 March 2026
Published: 19 March 2026

Abstract: Natural fibrous clays—sepiolite (SEP) and palygorskite (PLG)—were evaluated as sustainable photocatalysts for UV-C hydrogen generation from aqueous methanol solution. Native and 24 h pre-irradiated samples were characterized by gas quantification, FTIR, SEM, AAS, and zeta-potential measurements and compared with TiO_2 P25. PLG showed significant activation after irradiation: UV-C exposure removed carbonaceous residues and rearranged surface –OH groups, thereby improving channel accessibility and increasing H_2 evolution to values comparable to P25. In contrast, SEP hydroxylated more strongly after irradiation and formed robust hydrogen bonds that stabilized methanol-derived intermediates and temporarily suppressed activity, even though the crystal structure remained stable. The results show that SEP and PLG respond to UV-C through different surface chemistry mechanisms, rather than changes in the crystal lattice. PLG is activated by surface cleaning and reorganization of hydroxyls, while SEP is inhibited by stabilization of intermediates and excessive hydroxylation. Overall, fibrous silicates appear to be affordable, robust, and tunable photocatalysts whose performance can be controlled by surface cleanliness and hydration.

Keywords: sepiolite; palygorskite; fibrous clays; photocatalysis; hydrogen evolution

1. Introduction

The transition toward clean and sustainable energy solutions has placed photocatalytic technologies at the forefront of materials research, particularly in addressing challenges related to hydrogen generation and environmental remediation. Photocatalysis, a light-driven redox process capable of decomposing organic pollutants or producing molecular hydrogen, offers a promising strategy aligned with green chemistry principles [1,2]. However, much of the existing research has centered on engineered nanomaterials such as TiO_2, ZnO, or graphitic carbon nitride—materials that often require costly, energy-intensive synthesis, lack long-term stability, and involve complex post-synthetic modifications to achieve sufficient reactivity and selectivity [1–4].

In this context, naturally occurring clay minerals are gaining attention as earth-abundant, low-cost, sustainable, and environmentally benign photocatalysts. Among them, the fibrous magnesian phyllosilicates sepiolite and palygorskite—members of the same polysomatic series—combine high surface area, one-dimensional channels, and redox-active cations such as Fe^{3+}/Fe^{2+}. Both share a T–O–T (tetrahedral–octahedral–tetrahedral) ribbon framework, differing mainly in octahedral occupancy (trioctahedral sepiolite vs. dioctahedral palygorskite) but maintaining their fibrous morphology [5–9]. While long studied as hosts for semiconductor catalysts [10–13], recent work suggests that these clays can themselves contribute to photoinduced processes through their intrinsic structural and chemical features [2,14–16]. Their staggered 2:1 ribbon architecture,

composed of Mg-dominated octahedral sheets, forms open channels—six tetrahedra wide in sepiolite and four in palygorskite—connected by inverted tetrahedra through corner-sharing Si–O–Si bridges. This configuration preserves the continuity of the tetrahedral sheet, whereas the octahedral sheet remains discontinuous. This discontinuous octahedral connectivity and open-channel structure govern their high surface accessibility, hydration behavior, and photocatalytic performance [7,10,17,18].

Despite these promising observations, the intrinsic photocatalytic activity of natural fibrous clays remains poorly understood and significantly underexplored. To date, only a limited number of studies [2,14–16,19]—most of which focus on dye sensitization or involve hybridized systems—have systematically evaluated the behavior of unmodified palygorskite and sepiolite as standalone photocatalysts for pollutant degradation. Little is known about how their native properties, such as coordinated water, surface silanol groups, and redox-active transition metals, contribute to processes like photocatalytic methanol oxidation [2,14–16,20,21]. Addressing this gap will reveal how the clay matrix functions as a synergistically active component and enable clearer interpretation of clay-based hybrid photocatalysts.

In this work, we present a systematic investigation of unmodified sepiolite and palygorskite as standalone photocatalysts for hydrogen evolution from methanol–water solution under UV irradiation. Methanol was used as a model organic pollutant and as an efficient hole scavenger to evaluate the photocatalytic oxidation capability of the materials coupled with hydrogen evolution. Particular emphasis is placed on detailed structural and, especially, surface characterization, as these parameters fundamentally influence the photocatalytic response of fibrous clays. The results contribute to the growing recognition that such minerals are not merely passive supports, but can participate directly in photoinduced processes [14,16]. Accordingly, their intrinsic contribution should be explicitly considered when designing and evaluating clay-based composite photocatalysts. The novelty of this study lies in providing a control-validated evaluation of hydrogen evolution via methanol photoreforming over unmodified fibrous clays.

2. Materials and Methods

2.1. Materials

Two samples of natural fibrous clays (one sepiolite (SEP, Esquivias region, Madrid Basin, Spain) and one palygorskite (PLG, Lebrija area, Guadalquivir Basin, Spain)) were used as received from the supplier (Kremer Pigmente, Aichstetten, Germany), without any chemical modification and with an average grain size < 2 μm. No chemical pretreatment was applied to preserve their native mineralogical structure and chemical composition. Throughout this work, irradiated samples are denoted using the suffix _24H (_72H), referring to 24 h (72 h) of UV-C pretreatment under continuous irradiation. Samples irradiated in aqueous methanol are labeled accordingly (e.g., SEP_24H), whereas those irradiated in pure water are denoted with the suffix _Blank_24H (e.g., SEP_Blank_24H).

2.2. Characterization

Mineralogical composition was confirmed using X-ray powder diffraction (XRD, SmartLab, Rigaku, Akishima-shi, Tokyo, Japan) with Cu Kα radiation (λ = 1.5418 Å). Elemental composition was assessed by energy-dispersive X-ray fluorescence spectrometry (XRF, XEPOS, SPECTRO Analytical Instruments GmbH, Kleve, Germany) to obtain semiquantitative information on the major and minor elements present in the solid samples. Fourier-transform infrared spectroscopy (FTIR, iS10, Thermo Fisher Scientific, Waltham, MA, USA) was used to evaluate surface functionalities and structural OH groups. Scanning electron microscopy (SEM, Vega 3, Tescan Orsay Holding, Brno, Czechia) provided morphological insight into fiber architecture before and after irradiation; all micrographs were recorded under identical acquisition parameters (15 kV, SE + BSE, ~25 k×, WD ~ 11 mm). Atomic absorption spectroscopy (AAS, ContrAA, Analytik Jena GmbH + Co. KG, Jena, Germany) was used to assess leaching of framework cations after photocatalytic experiments. Zeta potential measurements (SZ-100V2 NanoPartica, HORIBA Scientific, Kyoto, Japan) were performed in 1 mM KCl solution in deionized water. UV-Vis diffuse reflectance spectroscopy (UV-Vis DRS; Specord 250 Plus, Analytik Jena GmbH + Co. KG, Jena, Germany) equipped with an integrating sphere was used to evaluate the optical response of the powder samples.

2.3. Photocatalytic Hydrogen Evolution Experiments

Photocatalytic H_2 evolution experiments were performed in a batch photoreactor (stainless steel, volume 305 cm^3). A detailed description of the photocatalytic experiment is provided in the Supplementary Materials.

2.4. Control and Post-Irradiation Analysis

Control experiments were performed in water-only systems (without methanol) under identical irradiation conditions to evaluate intrinsic photocatalytic activity in the absence of a sacrificial agent (methanol). After irradiation, the photocatalyst suspensions were clarified by centrifugation: first at 2500 rpm for 30 min to sediment coarse flocs—i.e., large aggregates of clay particles—then at 4000 rpm for 99 min to pellet the remaining fine powder. The obtained solid was washed with deionized water, centrifuged at 4000 rpm for 30 min and dried at 50 °C overnight in a laboratory oven. FTIR and SEM analyses were repeated to identify morphological alterations. The supernatant from centrifugation was collected for subsequent analysis. Leaching of Mg, Al, Fe, Ti and Mn into the solution was evaluated by AAS to assess structural integrity and possible photocorrosion effects.

3. Results and Discussion

3.1. X-Ray Diffraction (XRD) and X-Ray Fluorescence (XRF)

XRD pattern of native sepiolite (SEP) sample shows only sepiolite reflections with no additional crystalline phases resolved. By contrast palygorskite (PLG) sample is dominated by palygorskite with a minor sepiolite fraction (~80–85% PLG, ~15–20% SEP; semi-quantitative, possible preferred-orientation bias) and trace quartz and calcite. Diagnostic lines (Cu Kα, 2θ) include quartz at ~26.6°, calcite at ~29.4°, and a low-angle shoulder near ~7.4° attributable to SEP; the full XRD patterns and phase-markers are shown in Figure S3.

Bulk XRF cleanly separates the materials and matches their expected octahedral character. SEP is Mg-rich (MgO ≈ 23.3 wt%) and Al/Fe-poor (Al_2O_3 ≈ 2.1 wt%, Fe_2O_3 ≈ 0.8 wt%), consistent with trioctahedral sepiolite. PLG has more Al/Fe (Al_2O_3 ≈ 8.1 wt%, Fe_2O_3 ≈ 3.5 wt%) with moderate content of Mg (MgO ≈ 8.1 wt%); its elevated content of CaO (≈ 4.6 wt%) agrees with the calcite observed by XRD. A simple bulk proxy for octahedral type, MgO/(Al_2O_3 + Fe_2O_3), reinforces this reading: SEP ≈ 8.0 (Mg-rich, trioctahedral) versus PLG ≈ 0.67 (Al/Fe-enriched, dioctahedral [5,7,8].

Figure 1 compares the XRD patterns of the samples before and after irradiation. The diffraction profiles reveal that any observed modifications are confined to the surface and do not involve changes in the underlying crystalline framework. No shifts in basal reflections or broadening of principal peaks were detected, confirming that the structural integrity of the fibrous silicate lattice remains preserved. The only measurable alteration is the disappearance of calcite reflections in PLG following irradiation, observed in both aqueous methanol and water environments. This indicates preferential dissolution of minor carbonate impurities rather than framework degradation [22,23].

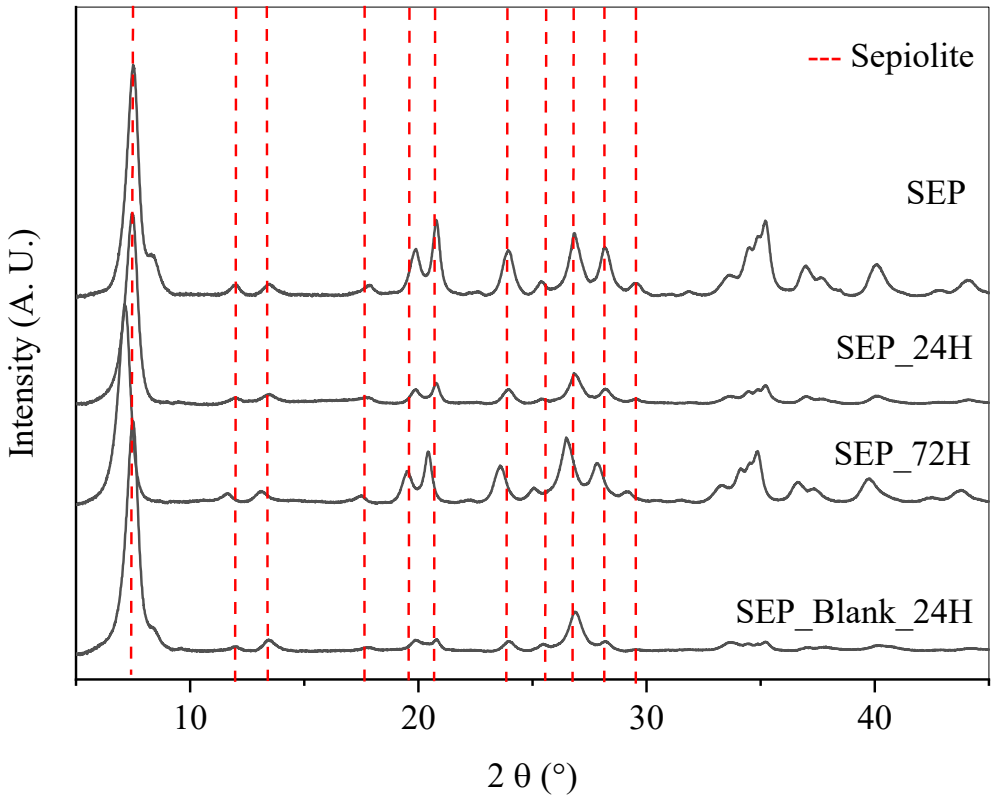

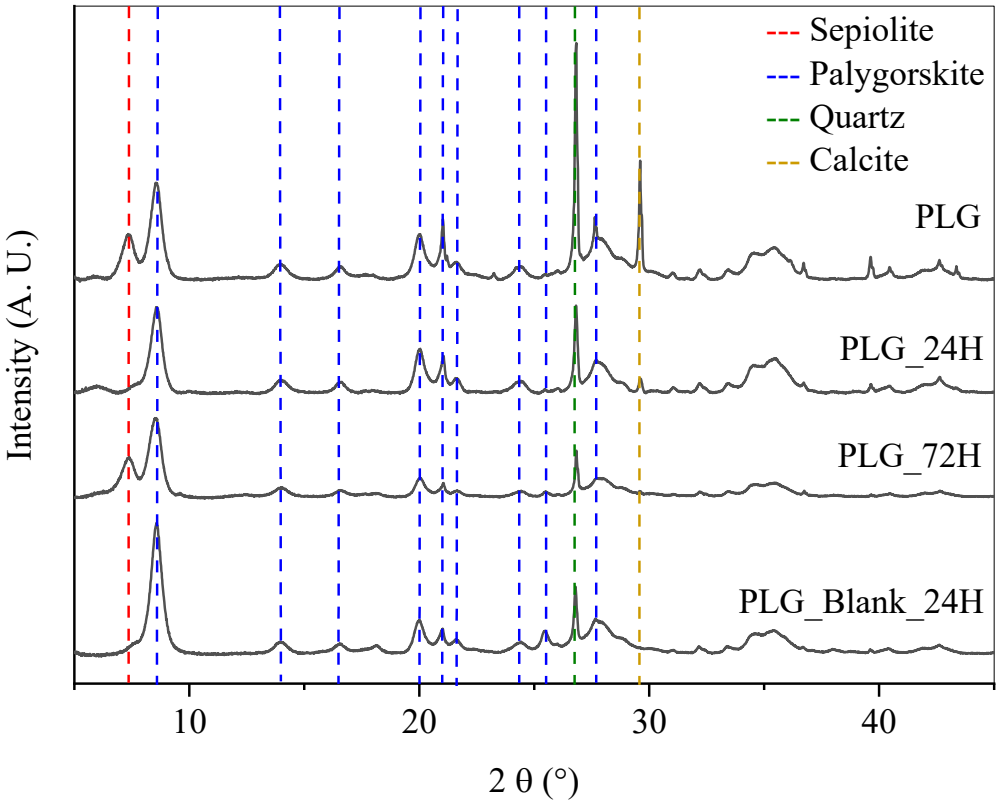

Figure 1. XRD patterns of sepiolite (**top**) and palygorskite (**bottom**) samples pre- and post UV-C treatment.

3.2. Fourier-Transform Infrared (FTIR) Spectrometry

FTIR tracks how the two fibrous clays respond to UV-C (254 nm) in aqueous methanol and water only solutions (Figure 2). Only diagnostic bands were evaluated: O–H stretching (3700–3000 cm^{-1}; sub-bands near ~3615, ~3548, 3450–3400, ~3300), C–H stretching (2960–2850 cm^{-1}), H–O–H bending (~1675–1630 cm^{-1}), Si–O stretching doublet (~1030/985 cm^{-1}), Si–OH/out-of-plane (~912 cm^{-1}) and lattice modes (≈600–450 cm^{-1}).

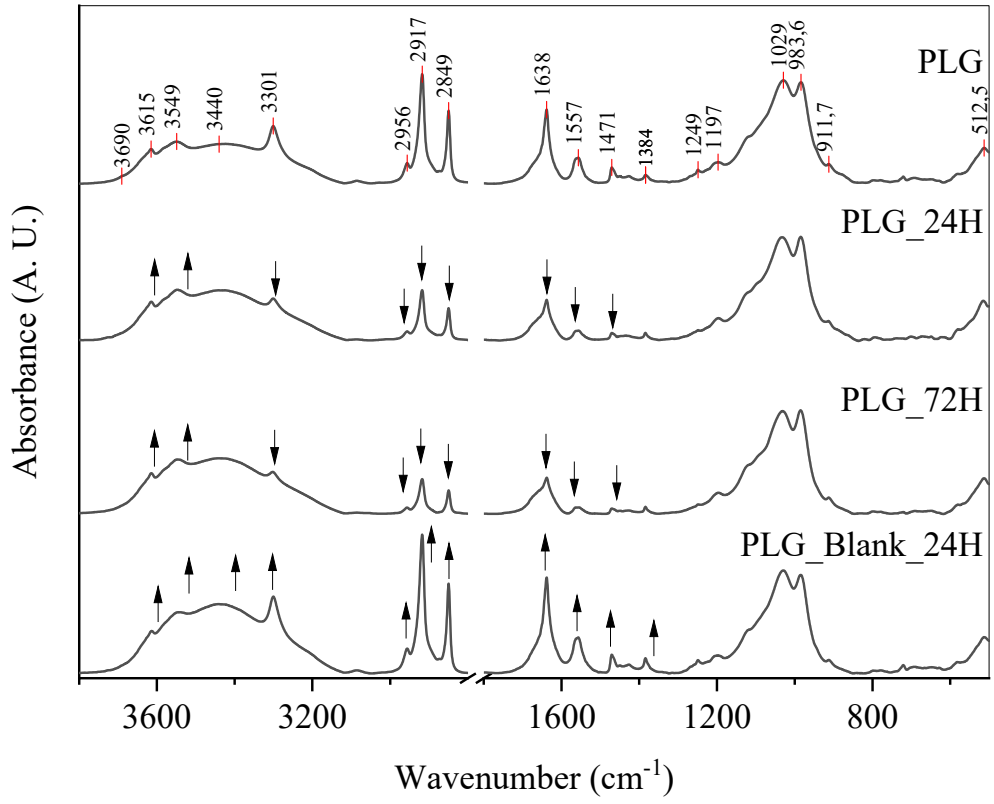

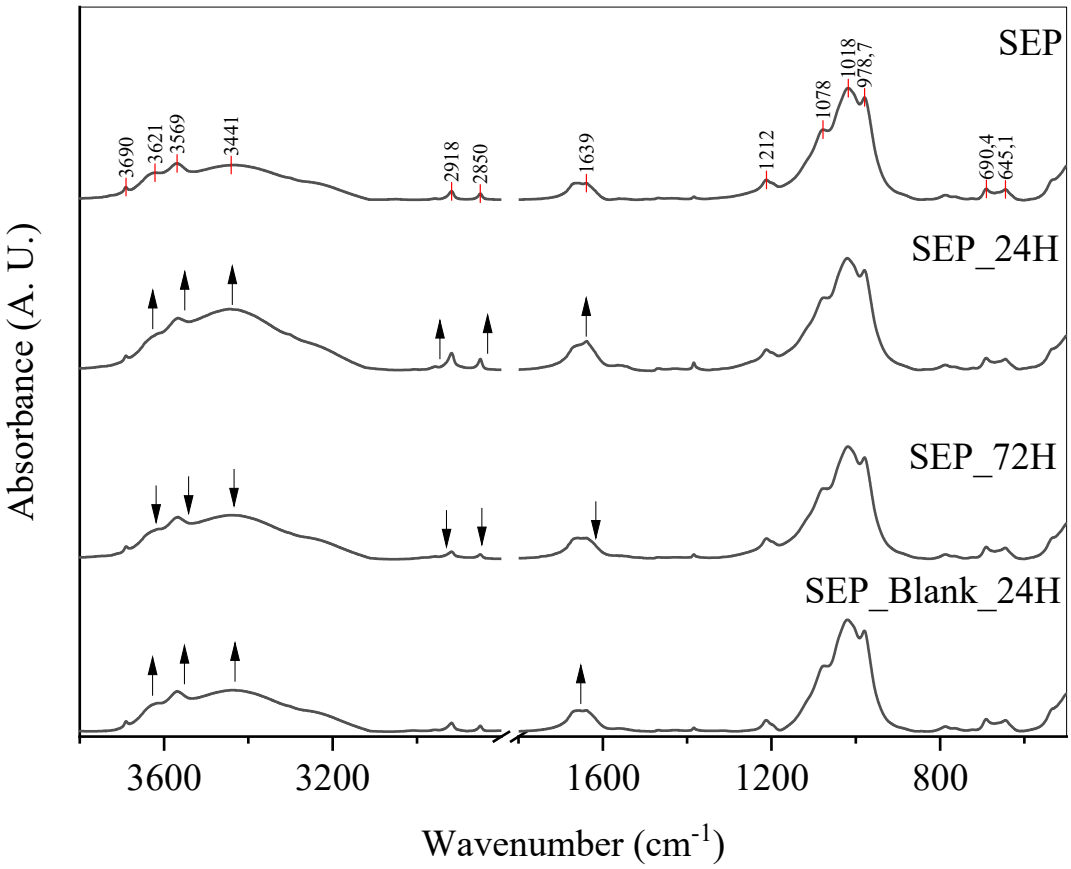

Figure 2. Transmission FTIR (KBr pellet) spectra of sepiolite (**top**) and palygorskite (**bottom**) before and after UV-C pretreatment. Spectra are normalised to the ν(Si–O) maximum at ≈1020 cm^{-1}. Arrows indicate trends of change as in comparison to spectrum of native samples.

Both clays maintain an intact silicate framework under UV-C in aqueous methanol (stable Si–O doublet and lattice bands) [24–29]. SEP responds reversibly: hydration and weak, transient C–H adsorption at 24 h relax toward native by 72 h. PLG shows persistent hydroxylation and marked C–H loss, consistent with surface cleaning in methanol; in water alone, both materials exhibit hydration without organic removal.

The ~3300 cm^{-1} contribution behaves as a dynamic probe of PLG tunnel-water ordering—intensified in water and diminished in methanol—whereas SEP lacks a resolvable 3300 cm^{-1} component [30–32].

Collectively, FTIR indicates that surface adsorption/hydration governs the spectral evolution, while the T–O–T ribbon architectures remain intact as confirmed by XRD; these trends are consistent with methanol-assisted radical processes that clean PLG surfaces and with largely reversible hydration in SEP. A detailed description of the FTIR spectra is provided in the Supplementary Materials.

3.3. Scanning Electron Microscopy (SEM)

3.3.1. Sepiolite (SEP)

Native SEP comprises straight, ribbon-like fibers organized in loosely packed, aligned bundles with broad inter-bundle voids and limited entanglement (Figure 3a), consistent with its narrow O–H envelope and low organic content in FTIR.

Under UV-C in aqueous methanol, the fibrous morphology remains largely intact: after 24 h, only minor abrasion and loosening occur, and by 72 h modest fraying and misalignment appear without fiber collapse (Figure 3b,c), paralleling a transient O–H increase followed by partial relaxation.

In water-only reference sample, SEP exhibits mild compaction and roughening but preserves its network structure (Figure 3d), consistent with the small, reversible FTIR hydration response. This overall resilience likely reflects its Mg-rich, trioctahedral framework and lower surface organic content compared with PLG [7,8].

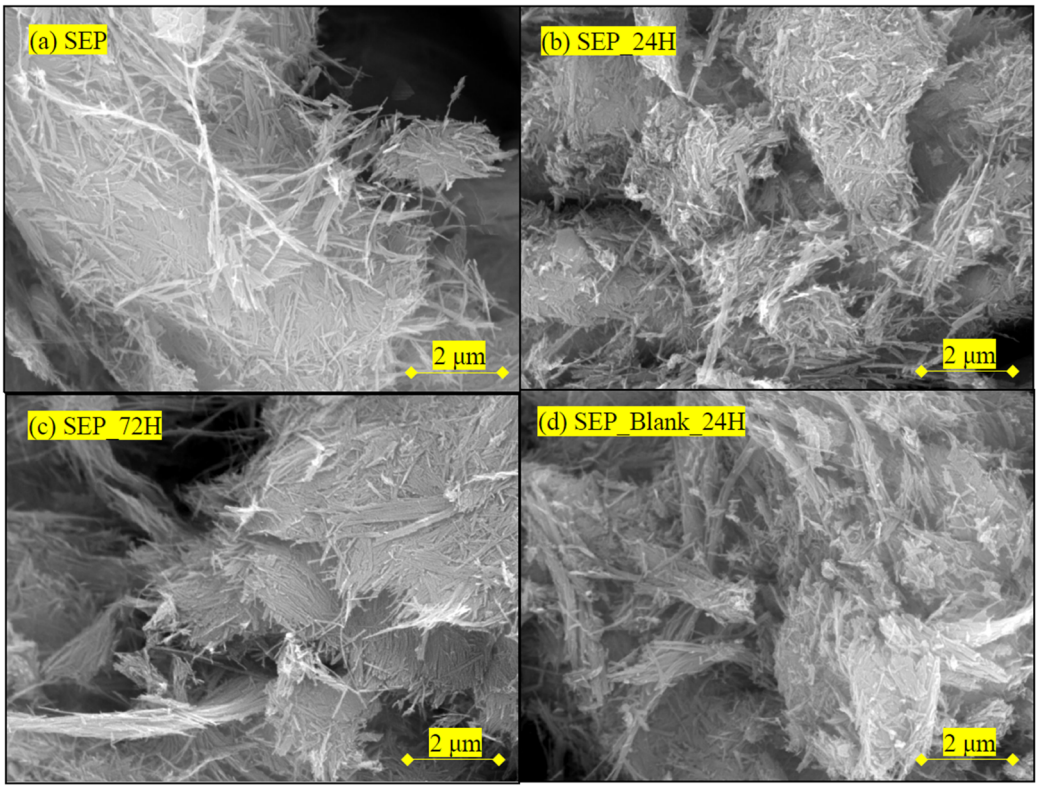

Figure 3. SEM morphology of sepiolite (SEP) before and after UV-C irradiation in aqueous methanol and in water-only blanks. (**a**) SEP, before irradiation; (**b**) SEP_24H; (**c**) SEP_72H; (**d**) SEP_Blank_24H.

3.3.2. Palygorskite (PLG)

Native PLG forms dense, highly entangled mats of rod-like fibers with frequent cross-linking and bundle intergrowths, creating a compact three-dimensional network (Figure 4a) consistent with its stronger organic FTIR signatures and broader O–H envelope.

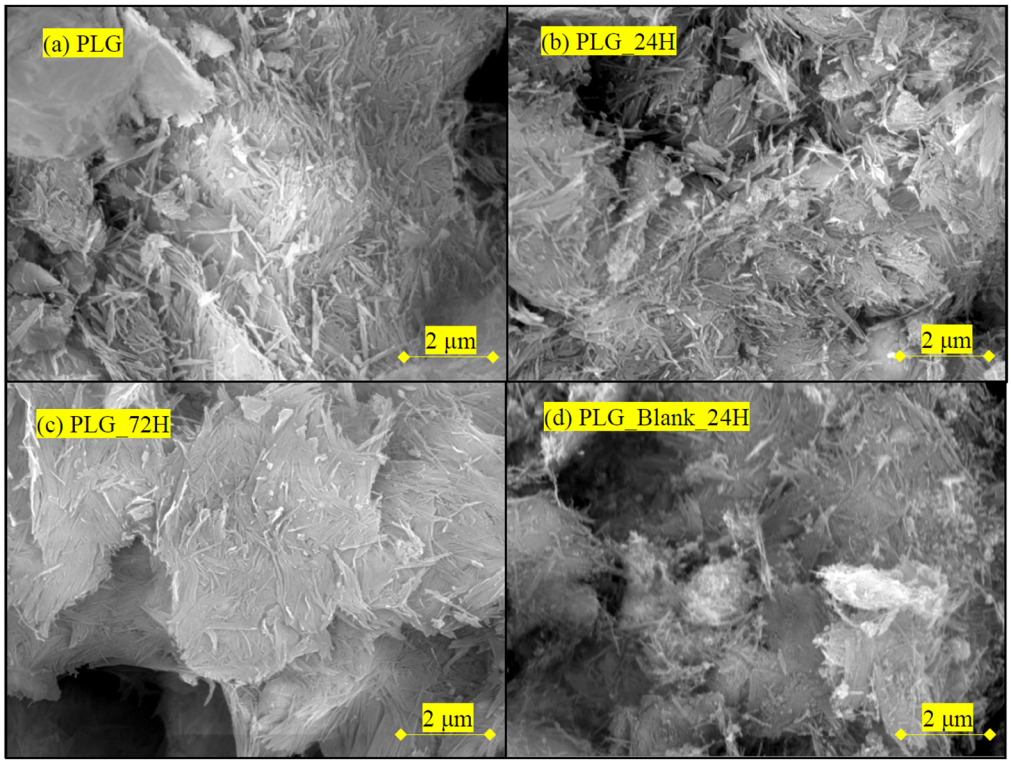

Figure 4. SEM morphology of palygorskite (PLG) before and after UV-C irradiation in aqueous methanol and in water-only blanks. (**a**) PLG, before irradiation; (**b**) PLG_24H; (**c**) PLG_72H; (**d**) PLG_Blank_24H.

Under UV-C in aqueous methanol, PLG shows pronounced surface abrasion, fibril roughening, and partial debundling after 24 h, progressing to locally compacted, planarized domains by 72 h (Figure 4b,c), indicative of partial loss or flattening of the fibrous texture rather than simple agglomeration. Limited Mg^{2+} release suggests leaching from edge sites, though other contributions cannot be excluded.

In water-only suspensions, PLG develops smooth, planarized films formed by bundle merging rather than debundling (Figure 4d), likely due to hydration-induced expansion followed by capillary collapse during drying. The FTIR response aligns with this: PLG exhibits the largest O–H increase in water (notably near 3300 cm^{-1}) and relatively persistent C–H signals, consistent with higher channel-water content and surface-organic retention. Overall, aqueous methanol promotes roughening and increased site accessibility, whereas water favours hydrated, planar films that may temporarily limit accessibility until reconditioned.

3.4. Zeta Potential (ζ)

Figure 5 shows that zeta potential was uniformly negative for all samples from pH 2 to 12, indicating an isoelectric point below the tested range and a surface dominated by deprotonated silanol and edge –M–OH sites [33–35]. Since the photocatalytic experiments operate within pH 5–7, this region is particularly relevant: here, SEP shows a modest decrease in ζ magnitude after 24 h UV-C exposure, indicating partial charge relaxation likely linked to changes in surface coverage or specific-ion adsorption rather than residual organics [33,36,37]. In contrast, PLG becomes more negatively charged in this same pH window after irradiation, shifting its electrostatic stability threshold ($|\zeta| \gtrsim 30$ mV) toward near-neutral conditions. This behavior aligns with FTIR evidence of surface cleaning and rehydration that expose additional $–SiO^-$/$–MO^-$ sites, enhancing dispersion and accessibility under the conditions of hydrogen-evolution testing.

These electrostatic trends reflect distinct charge-regulation mechanisms in the two clays: SEP shows ζ-potential relaxation at higher pH due to stronger surface coverage and charge compensation, whereas PLG retains a more negative, stable ζ-potential, indicating better dispersion and greater surface-site accessibility [33–35,37]. These differences align with their microstructural variability—fiber length, porosity, and channel accessibility—which dictate the density and reactivity of terminal –OH groups [9,35,37,38].

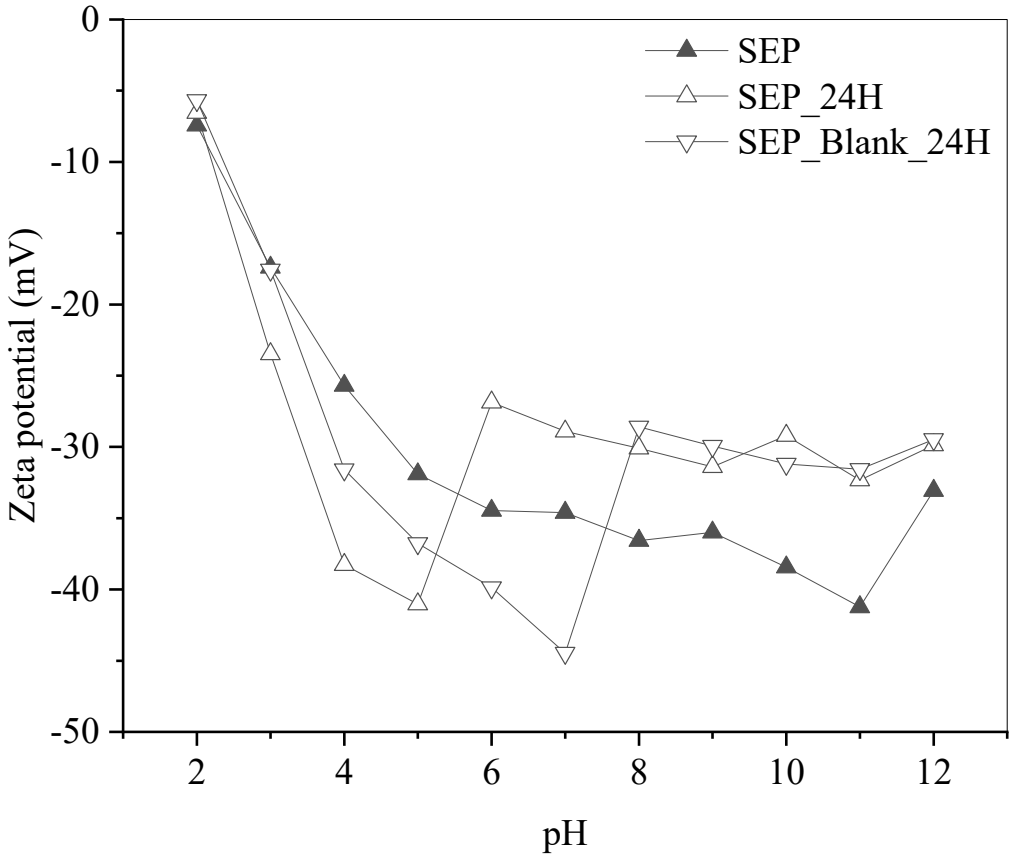

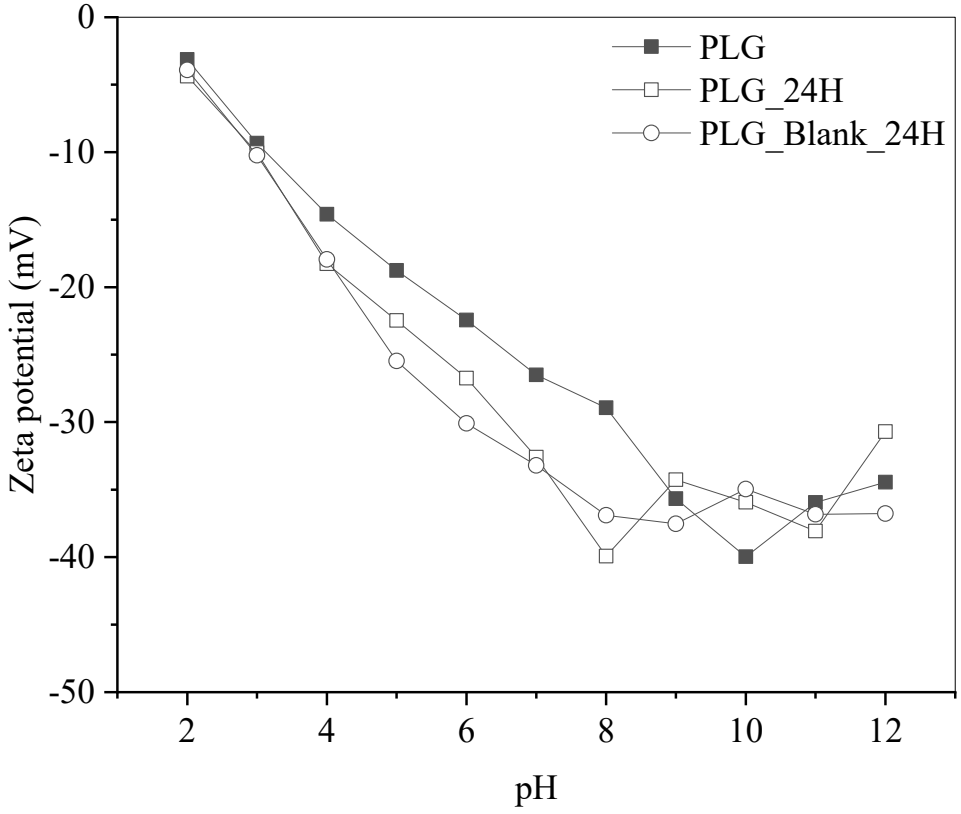

Figure 5. Zeta potential of sepiolite (**top**) and palygorskite (**bottom**) samples as a function of pH measured in 1 mM KCl solution.

3.5. Atomic Absorption Spectrometry (AAS)

AAS supports the FTIR and SEM results, confirming distinct differences in chemical resilience (Figure 6). In SEP, Mg leaching proceeds more slowly and linearly (0.66 → 0.94 mg/L) under irradiation in methanol solution, indicating higher structural stability. Comparable Mg levels in water control (0.87 mg/L) suggest that Mg release is mainly governed by hydration rather than photocatalytic oxidation. This indicates that Mg is more surface-accessible or loosely bound without signs of deeper structural decomposition.

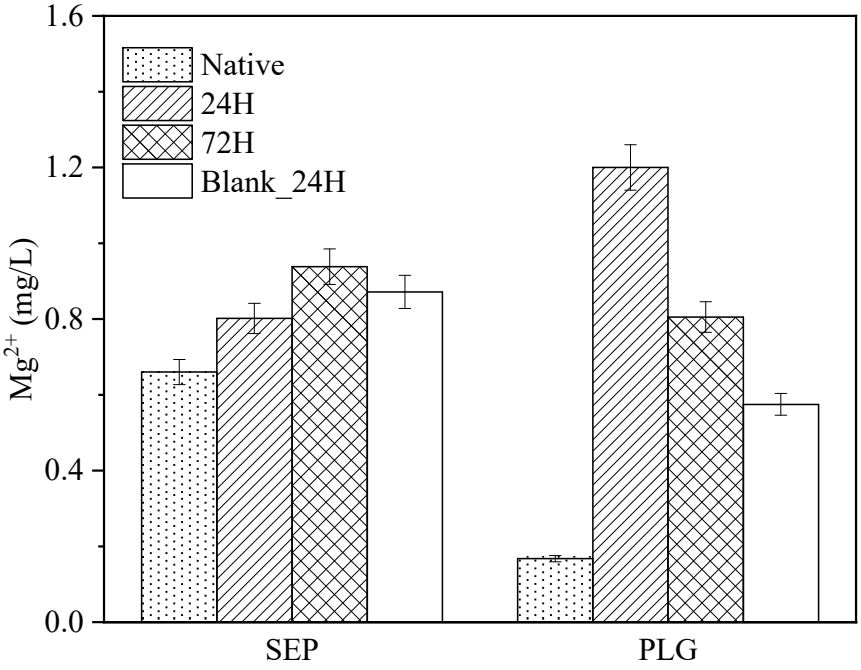

Figure 6. Mg^{2+} leaching from palygorskite (PLG) and sepiolite (SEP) post UV irradiation.

In contrast, PLG shows a sharp increase in Mg leaching after 24 h irradiation in methanol solution (1.20 mg/L), coinciding with visible morphological degradation and attenuation of organic signals. This behavior indicates the release of structurally bound Mg^{2+} from octahedral layers due to framework disruption and oxidative degradation.

No detectable leaching of Al (<0.59 mg/L), Fe (<0.16 mg/L), Mn (<0.04 mg/L), or Ti (<1.44 mg/L) was observed in any sample, underscoring the chemical robustness of the core clay matrices.

3.6. UV-Vis Diffuse Reflectance

Diffuse reflectance UV-Vis spectra (UV-Vis DRS) of powdered sepiolite (SEP) and palygorskite (PLG) were recorded and expressed as the Kubelka–Munk function, $F(R_\infty) = (1-R)^2/(2R)$, as a pseudo-absorbance descriptor for diffusely scattering, optically thick powders. Both materials show a dominant UV absorption edge (onset ~4.0 eV; maximum slope ~4.4–4.5 eV) together with a weaker near-UV contribution around ~3.3 eV, superimposed on the main edge. For comparison, two characteristic energies were extracted from Tauc-type linear constructions: a low-energy sub-gap threshold of ~2.0 eV for SEP and ~2.3 eV for PLG, and a higher-energy apparent edge at ~3.7 eV for SEP and ~3.5 eV for PLG (baseline-intersection). Because $F(R_\infty)$ represents the absorption-to-scattering ratio and natural clays commonly exhibit sub-band-gap absorption tails due to compositional heterogeneity and transition-metal-related charge-transfer and defect states, these values are discussed conservatively as apparent (model-dependent) optical thresholds rather than unique intrinsic band gaps of the phyllosilicate framework. This interpretation is consistent with complementary characterization: XRD shows only sepiolite reflections for SEP, whereas PLG is dominated by palygorskite with minor sepiolite and trace quartz and calcite, and bulk XRF indicates substantially higher Fe content in PLG (Fe_2O_3 ≈ 3.5 wt%) than in SEP (Fe_2O_3 ≈ 0.8 wt%), which may enhance sub-gap absorption [39–41].

3.7. Photocatalytic Methanol Reforming

3.7.1. Hydrogen Evolution

After 4 h of UV-C irradiation, both clay matrices exhibit different behavior depending on the medium used (Figure 7).

In methanol solution (Figure 7, top), the hydrogen yield decreases for SEP (from 518 to 352 μmol·g_{cat}^{-1}), while it increases significantly for PLG (from 347 to 564 μmol·g_{cat}^{-1}), indicating different stability and photocatalytic activation capacity after preliminary irradiation. The corresponding time-dependent hydrogen evolution profiles are shown in Figure S5.

In control experiments with water, the trend is reversed (Figure 7, bottom). SEP activity increases slightly (from 52 to 77 μmol·g_{cat}^{-1}), while PLG activity decreases significantly (from 69 to 8 μmol·g_{cat}^{-1}). This suggests that SEP is dominated by an adsorption effect associated with hydration, while PLG undergoes true photocatalytic activation only in the presence of methanol.

The significantly higher H_2 evolution observed in the methanol–water system compared to pure water indicates that the dominant pathway is photocatalytic oxidation of methanol coupled with proton reduction. Therefore, these experiments should not be interpreted as overall water splitting, but rather as photocatalytic methanol reforming or organic oxidation accompanied by hydrogen evolution.

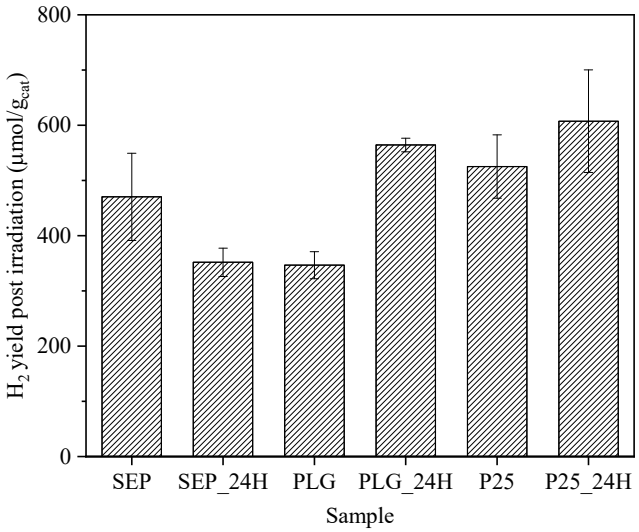

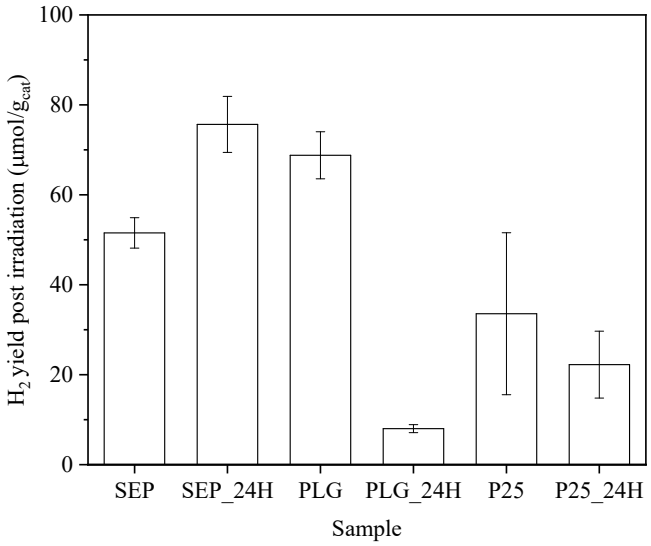

Figure 7. Comparison of total hydrogen yields obtained after 4 h from the same photocatalysts in aqueous methanol (**top**) and water (**bottom**).

Compared to the reference TiO_2 P25, PLG achieves a comparable level of activity after conditioning, while control samples in water confirm that H_2 formation is due to photoexcitation and not the presence of organic residues. In tests in the dark (blank tests), no hydrogen formation was detected, which rules out the formation of reactive oxygen species under these conditions [42–44].

3.7.2. Effect of Pre-Irradiation in Aqueous Methanol

After 24 h of continuous UV-C irradiation, SEP exhibits a broader, more intense O–H envelope (3600–3000 cm^{-1}) together with a modest C–H increase, while XRD shows unchanged peak positions—consistent with surface reconditioning rather than a lattice change. These observations suggest (i) a denser interfacial H-bond network that may stabilize intermediates (methoxy/formate-like) at reactive Mg–OH/Si–OH/Lewis sites [45–47]; (ii) more persistent adsorption of methanol-derived fragments that could partially occupy or slow access to those sites [45,47]; and (iii) re-wetting/thicker solvation shells in channels, that hinder methanol/CO_x transport and product desorption [46,48]. Collectively, these effects (iv) increase the proton-donating/H-bonding propensity of surface –OH groups, favoring intermediate confinement and partial back-oxidation [45,47] over rapid H_2 evolution—consistent with the lower H_2 yield observed in aqueous methanol.

UV-C pretreatment leaves PLG with a cleaner, less water-clogged surface (attenuated C–H envelope, weaker ~3300 cm^{-1} H-bonded H_2O; mild fiber roughening/debundling without lattice change). Together, these trends support several coupled effects: (i) degradation of native organics (attenuation of intensity in FTIR C–H vibration region), unblocking Lewis/Brønsted sites [14]; (ii) channel-water reorganization, reducing competitive H-bonding in tunnels and improving methanol access [18,46–48]; (iii) partial removal of adsorbate or defect state that my otherwise promote e^-/h^+ recombination [49–51]; (iv) UV-C exposure likely cleans and reconditions surface, exposing –OH/Lewis sites. These sites can facilitate proton-coupled electron transfer with methanol and thus improve hole scavenging [47,52–54].

In aqueous methanol, methanol acts as a sacrificial hole donor. It first adsorbs and deprotonates at oxide/Lewis sites, forming surface methoxy (CH_3O^-), which serves as the dominant hole-reactive adsorbate under UV irradiation. The adsorbed methoxy species is then oxidized stepwise (often via $CH_3O•$ or $CH_2OH•$ radicals) toward formaldehyde and formate, releasing protons that are reduced by conduction band electrons to H_2 ($2H^+ + 2e^- \rightarrow H_2$). The volatile carbon products arise mainly from oxidative steps (methanol → HCHO → formate), with CO occasionally detected via formate decomposition. When sufficiently reducing or co-catalyzed sites are present, adsorbed CO may be further hydrogenated to CH_4 [45,47,55].

In water-only runs, photogenerated h^+/•OH species preferentially attack intrinsic organics. Within this mechanistic context, PLG_24H behaves as a cleaned and mildly dehydrated-channel surface. Adventitious carbonaceous residues are removed, channel water is partially reorganized or expelled, and active sites become more accessible. These changes likely reduce the density of recombination active surface states—consistent with higher H_2 yield observed. By contrast, SEP_24H becomes more hydroxylated and strongly hydrogen-bonding,

which stabilizes methanol-derived intermediates and slows their conversion; in aqueous methanol this manifests as lower H_2 yield.

When benchmarked against TiO_2 P25, the two clays exhibit complementary behaviors. SEP reaches P25-level H_2 yields in its native, unconditioned state. However, its activity decreases after pre-irradiation, suggesting that surface processes dominate its response. The reduced resilience of SEP may result from intermediate adsorption and subsequent site blocking, where surface hydroxyl groups stabilize methanol-derived species through hydrogen bonding or condensation reactions. This interaction hinders further charge transfer. In contrast, PLG shows the opposite trend. Its activity increases after conditioning, and post-irradiation yields approach those of P25, indicating progressive activation of surface sites and improved interfacial charge separation. Thus, while both clays can transiently match benchmark activity, their mechanistic pathways diverge: SEP undergoes surface saturation, whereas PLG experiences progressive surface activation.

4. Conclusions

Natural fibrous clays (palygorskite (PLG) and sepiolite (SEP)) exhibit intrinsic photocatalytic activity in UV-C hydrogen generation from aqueous methanol solutions even without additional cocatalysts. Powder XRD measurements confirm the stability of the crystal lattice in both original and irradiated samples, indicating that changes in activity are due to surface reorganization rather than structural transformations. FTIR and SEM show that 24-h UV-C exposure in aqueous methanol cleans and reconstitutes the PLG surface, removing carbonaceous residues and rearranging –OH groups, which opens channels and enhances charge separation. In contrast, SEP shows increased hydroxylation and stronger hydrogen bonds, which stabilize methanol-derived intermediates and temporarily reduce activity. Overall, the photocatalytic behavior of these clays is determined more by surface hydration and coverage with native organics than by their crystal structure. Fibrous silicates thus emerge as tunable and affordable photocatalysts whose performance is primarily controlled by surface chemistry. Controlling surface cleanliness and hydration therefore represents a direct way to influence hydrogen evolution. The results further demonstrate the potential of unmodified sepiolite and palygorskite for photocatalytic oxidation of organic pollutants in water with simultaneous hydrogen generation under UV irradiation.

Supplementary Materials

The additional data and information can be downloaded at: https://media.sciltp.com/articles/others/260319107206116/Photocatalysis-SM-26010109-FC-done.pdf. Figure S1: Emission spectrum of the UVP Pen-Ray® low-pressure mercury lamp employed in this study. Figure S2: Time-dependent hydrogen evolution during photolysis and photocatalysis in aqueous methanol (A) and water (B) under continuous UV-C irradiation ($\lambda = 254$ nm) and comparison of total hydrogen yields obtained after 4 h in case of photolysis and photocatalysis in aqueous methanol (C) and water (D). Figure S3: Powder X-ray diffraction patterns of natural sepiolite (SEP) and palygorskite (PLG) sample (C-calcite, P-palygorskite, Q-quartz, S-sepiolite). Figure S4: Tauc plots for sepiolite (SEP, black) and palygorskite (PLG, red) derived from UV-Vis DRS illustrating the evaluation of apparent (model-dependent) optical gap parameters. Figure S5: Time-dependent hydrogen evolution of sepiolite (SEP), palygorskite (PLG), and TiO_2 (P25) photocatalysts before and after 24 h of UV-C pretreatment (24 h) in aqueous methanol under continuous irradiation. References [56–64] are cited in supplementary materials.

Author Contributions

P.K.: investigation, conceptualization, methodology, validation, writing—reviewing and editing; A.M.: investigation, conceptualization, methodology; K.K.: conceptualization, methodology, validation, writing—reviewing and editing, supervision. All authors have read and agreed to the published version of the manuscript.

Funding

This work was supported by the Large Research Infrastructure ENREGAT (projects No. LM2023056 and LM2018098) and by the European Union under the REFRESH—Research Excellence for REgion Sustainability and High-tech Industries project (No. CZ.10.03.01/00/22_003/0000048) via the Operational Program Just Transition.

Data Availability Statement

The data is available at this link: https://doi.org/10.5281/zenodo.17606418.

Acknowledgments

The authors are grateful to Kamil Maciej Górecki for SEM, XRF, and FTIR measurements, Adam Hruška for AAS analyses, and Jan Bednárek for ζ-potential and UV-Vis DRS measurements. An earlier version of our work has been published online as a preprint via the Research Square platform with DOI: https://doi.org/10.21203/rs.3.rs-8173007/v1.

Conflicts of Interest

The authors declare no conflict of interest.

Use of AI and AI-Assisted Technologies

During the preparation of this work, the authors used Chat GPT for language editing purposes. After using this tool/service, the authors reviewed and edited the content as needed and take full responsibility for the content of the published article.

References

1. Beil, S.B.; Bonnet, S.; Casadevall, C.; et al. Challenges and Future Perspectives in Photocatalysis: Conclusions from an Interdisciplinary Workshop. *JACS Au* **2024**, *4*, 2746–2766. https://doi.org/10.1021/jacsau.4c00527.
2. Mohamed, H.H.; Wazan, G.; Besisa, D.H.A. Natural Clay Minerals as Heterojunctions of Multi-Metal Oxides for Superior Photocatalytic Activity. *Mater. Sci. Eng. B* **2022**, *286*, 116077. https://doi.org/10.1016/j.mseb.2022.116077.
3. Ahmad, I.; Zou, Y.; Yan, J.; et al. Semiconductor Photocatalysts: A Critical Review Highlighting the Various Strategies to Boost the Photocatalytic Performances for Diverse Applications. *Adv. Colloid Interface Sci.* **2023**, *311*, 102830. https://doi.org/10.1016/j.cis.2022.102830.
4. Aboualigaledari, N.; Rahmani, M. A Review on the Synthesis of the TiO_2-Based Photocatalyst for the Environmental Purification. *J. Compos. Compd.* **2021**, *3*, 25–42. https://doi.org/10.52547/jcc.3.1.4.
5. Suárez, M.; García-Romero, E. Sepiolite-Palygorskite: A Continuous Polysomatic Series. *Clays Clay Miner.* **2013**, *61*, 461–472. https://doi.org/10.1346/CCMN.2013.0610505.
6. Cecilia, J.A.; Vilarrasa-García, E.; Cavalcante, C.L.; et al. Evaluation of Two Fibrous Clay Minerals (Sepiolite and Palygorskite) for CO_2 Capture. *J. Environ. Chem. Eng.* **2018**, *6*, 4573–4587. https://doi.org/10.1016/j.jece.2018.07.001.
7. Pozo, M.; Calvo, J.P. An Overview of Authigenic Magnesian Clays. *Minerals* **2018**, *8*, 520. https://doi.org/10.3390/min8110520.
8. Herranz, J.; Pozo, M. Sepiolite and Other Authigenic Mg-Clay Minerals Formation in Different Palustrine Environments (Madrid Basin, Spain). *Minerals* **2022**, *12*, 987. https://doi.org/10.3390/min12080987.
9. Suárez, M.; García-Rivas, J.; Morales, J.; et al. Review and New Data on the Surface Properties of Palygorskite: A Comparative Study. *Appl. Clay Sci.* **2022**, *216*, 106311. https://doi.org/10.1016/j.clay.2021.106311.
10. Serwicka, E.M. Titania-Clay Mineral Composites for Environmental Catalysis and Photocatalysis. *Catalysts* **2021**, *11*, 1087. https://doi.org/10.3390/catal11091087.
11. Freitas, W.; Trigueiro, P.; Marinho, T.; et al. The Role of Clay Mineral-Derived Photocatalysts in Insights of Remediation. *Ceramics* **2022**, *5*, 862–882. https://doi.org/10.3390/ceramics5040063.
12. Heidari, A.; Shahbazi, A.; Aminabhavi, T.M.; et al. A Systematic Review of Clay-Based Photocatalysts for Emergent Micropollutants Removal and Microbial Inactivation from Aqueous Media: Status and Limitations. *J. Environ. Chem. Eng.* **2022**, *10*, 108813. https://doi.org/10.1016/j.jece.2022.108813.
13. Chuaicham, C.; Trakulmututa, J.; Shu, K.; et al. Recent Clay-Based Photocatalysts for Wastewater Treatment. *Separations* **2023**, *10*, 77. https://doi.org/10.3390/separations10020077.
14. Valášková, M.; Filip Edelmannová, M.; Reli, M.; et al. New Evidence for the Photocatalytic Efficiency of Natural Raw Vermiculites to Produce Hydrogen from Aqueous Methanol Solution. *Heliyon* **2025**, *11*, e42366. https://doi.org/10.1016/j.heliyon.2025.e42366.
15. Liu, Z.; Wang, J.; Ma, H.; et al. A New Natural Layered Clay Mineral Applicable to Photocatalytic Hydrogen Production and/or Degradation of Dye Pollutant. *Environ. Prog. Sustain. Energy* **2018**, *37*, 1003–1010. https://doi.org/10.1002/ep.12775.
16. Mubiayi, M.P.; Muleja, A.A.; Nzaba, S.K.M.; et al. Geochemical and Physicochemical Characteristics of Clay Materials from Congo with Photocatalytic Activity on 4-Nitrophenol in Aqueous Solutions. *ACS Omega* **2020**, *5*, 29943–29954. https://doi.org/10.1021/acsomega.0c04295.
17. Galan, E. Properties and Applications of Palygorskite-Sepiolite Clays. *Clay Miner.* **1996**, *31*, 443–453. https://doi.org/10.1180/claymin.1996.031.4.01.

18. Almeida, R.; Ferraz, E.; Santarén, J.; et al. Comparison of Surface Properties of Sepiolite and Palygorskite: Surface Energy and Nanoroughness. *Nanomaterials* **2021**, *11*, 1579. https://doi.org/10.3390/nano11061579.
19. Zhang, J.; Liu, T.; Chen, R.; et al. Vermiculite as a Natural Silicate Crystal for Hydrogen Generation from Photocatalytic Splitting of Water under Visible Light. *RSC Adv.* **2014**, *4*, 406–408. https://doi.org/10.1039/C3RA45301D.
20. Bañuelos, J.L.; Borguet, E.U.; Brown, G.E.; et al. Oxide- and Silicate-Water Interfaces and Their Roles in Technology and the Environment. *Chem. Rev.* **2023**, *123*, 6413–6544. https://doi.org/10.1021/acs.chemrev.2c00130.
21. Gournis, D.; Karakassides, M.A.; Petridis, D. Formation of Hydroxyl Radicals Catalyzed by Clay Surfaces. *Phys. Chem. Miner.* **2002**, *29*, 155–158. https://doi.org/10.1007/s002690100215.
22. Basheer, C.; Rashwan, M.; Al-Mutairi, E.; et al. Application of Ultraviolet Radiation to Control the Calcium Carbonate Scale Formation and Deposition on the Membranes. *J. Chem.* **2020**, *2020*, 8083705. https://doi.org/10.1155/2020/8083705.
23. Kabacińska, Z.; Krzyminiewski, R.; Tadyszak, K.; et al. Generation of UV-Induced Radiation Defects in Calcite. *Quat. Geochronol.* **2019**, *51*, 24–42. https://doi.org/10.1016/j.quageo.2019.01.002.
24. Madejová, J.; Gates, W.P.; Petit, S. IR Spectra of Clay Minerals. In *Developments in Clay Science*; Elsevier: Amsterdam, The Netherlands, 2017; Volume 8, pp. 107–149. https://doi.org/10.1016/B978-0-08-100355-8.00005-9.
25. Lescano, L.; Castillo, L.; Marfil, S.; et al. Alternative Methodologies for Sepiolite Defibering. *Appl. Clay Sci.* **2014**, *95*, 378–382. https://doi.org/10.1016/j.clay.2014.05.001.
26. Bukas, V.J.; Tsampodimou, M.; Gionis, V.; et al. Synchronous ATR Infrared and NIR-Spectroscopy Investigation of Sepiolite upon Drying. *Vib. Spectrosc.* **2013**, *68*, 51–60. https://doi.org/10.1016/j.vibspec.2013.05.009.
27. Frost, R.L.; Locos, O.B.; Ruan, H.; et al. Near-Infrared and Mid-Infrared Spectroscopic Study of Sepiolites and Palygorskites. *Vib. Spectrosc.* **2001**, *27*, 1–13. https://doi.org/10.1016/S0924-2031(01)00110-2.
28. Gionis, V. On the Structure of Palygorskite by Mid- and Near-Infrared Spectroscopy. *Am. Mineral.* **2006**, *91*, 1125–1133. https://doi.org/10.2138/am.2006.2023.
29. McKeown, D.A.; Post, J.E.; Etz, E.S. Vibrational Analysis of Palygorskite and Sepiolite. *Clays Clay Miner.* **2002**, *50*, 667–680. https://doi.org/10.1346/000986002320679549.
30. Suárez, M.; García-Romero, E. FTIR Spectroscopic Study of Palygorskite: Influence of the Composition of the Octahedral Sheet. *Appl. Clay Sci.* **2006**, *31*, 154–163. https://doi.org/10.1016/j.clay.2005.10.005.
31. Frost, R.L.; Cash, G.A.; Kloprogge, J.T. 'Rocky Mountain Leather', Sepiolite and Attapulgite—An Infrared Emission Spectroscopic Study. *Vib. Spectrosc.* **1998**, *16*, 173–184. https://doi.org/10.1016/S0924-2031(98)00014-9.
32. Liu, Q.; Yao, X.; Cheng, H.; et al. An Infrared Spectroscopic Comparison of Four Chinese Palygorskites. *Spectrochim. Acta Part A* **2012**, *96*, 784–789. https://doi.org/10.1016/j.saa.2012.07.025.
33. Alkan, M.; Demirbaş, Ö.; Doğan, M. Electrokinetic Properties of Sepiolite Suspensions in Different Electrolyte Media. *J. Colloid Interface Sci.* **2005**, *281*, 240–248. https://doi.org/10.1016/j.jcis.2004.08.036.
34. Chen, C.; Wang, F.; Liang, J.S.; et al. Zeta Potential of Sepiolite in Aqueous System. *Adv. Mater. Res.* **2012**, *427*, 208–211. https://doi.org/10.4028/www.scientific.net/AMR.427.208.
35. Serrano-Lotina, A.; Portela, R.; Baeza, P.; et al. Zeta Potential as a Tool for Functional Materials Development. *Catal. Today* **2023**, *423*, 113862. https://doi.org/10.1016/j.cattod.2022.08.004.
36. Neaman, A.; Singer, A. Rheological Properties of Aqueous Suspensions of Palygorskite. *Soil Sci. Soc. Am. J.* **2000**, *64*, 427–436. https://doi.org/10.2136/sssaj2000.641427x.
37. Ferraz, E.; Alves, L.; Sanguino, P.; et al. Stabilization of Palygorskite Aqueous Suspensions Using Bio-Based and Synthetic Polyelectrolytes. *Polymers* **2020**, *13*, 129. https://doi.org/10.3390/polym13010129.
38. Suárez, M.; García-Romero, E. Variability of the Surface Properties of Sepiolite. *Appl. Clay Sci.* **2012**, *67–68*, 72–82. https://doi.org/10.1016/j.clay.2012.06.003.
39. Klein, J.; Kampermann, L.; Mockenhaupt, B.; et al. Limitations of the Tauc Plot Method. *Adv. Funct. Mater.* **2023**, *33*, 2304523. https://doi.org/10.1002/adfm.202304523.
40. Makuła, P.; Pacia, M.; Macyk, W. How To Correctly Determine the Band Gap Energy of Modified Semiconductor Photocatalysts Based on UV-Vis Spectra. *J. Phys. Chem. Lett.* **2018**, *9*, 6814–6817. https://doi.org/10.1021/acs.jpclett.8b02892.
41. Pham, H.; Neves, J.C.; Yan, R.; et al. Improving Bandgap Determination by Optical Spectroscopy: Comparative Evaluation of ISARS, UV-Vis, and Diffuse Reflectance. *ACS Meas. Sci. Au* **2025**, *5*, 666–676. https://doi.org/10.1021/acsmeasuresciau.5c00059.
42. Yu, C.; Lu, Y.; Zhang, Y.; et al. Significant Contribution of Solid Organic Matter for Hydroxyl Radical Production during Oxygenation. *Environ. Sci. Technol.* **2022**, *56*, 11878–11887. https://doi.org/10.1021/acs.est.2c02766.
43. Du, H.; Cao, Y.; Li, Z.; et al. Formation and Mechanisms of Hydroxyl Radicals during the Oxygenation of Sediments in Lake Poyang, China. *Water Res.* **2021**, *202*, 117442. https://doi.org/10.1016/j.watres.2021.117442.
44. Page, S.E.; Kling, G.W.; Sander, M.; et al. Dark Formation of Hydroxyl Radical in Arctic Soil and Surface Waters. *Environ. Sci. Technol.* **2013**, *47*, 12860–12867. https://doi.org/10.1021/es4033265.

45. Panayotov, D.A.; Burrows, S.P.; Morris, J.R. Photooxidation Mechanism of Methanol on Rutile TiO_2 Nanoparticles. *J. Phys. Chem. C* **2012**, *116*, 6623–6635. https://doi.org/10.1021/jp209215c.
46. Zhurka, M.D.; Anderson, J.A.; McCue, A.J.; et al. Investigation of Support Effects during Ethanol Steam Reforming over a Ni/Sepiolite Catalyst. *React. Chem. Eng.* **2023**, *8*, 2984–2999. https://doi.org/10.1039/D3RE00181D.
47. Setvin, M.; Shi, X.; Hulva, J.; et al. Methanol on Anatase TiO_2 (101): Mechanistic Insights into Photocatalysis. *ACS Catal.* **2017**, *7*, 7081–7091. https://doi.org/10.1021/acscatal.7b02003.
48. Hijazi, N.; Bavykina, A.; Yarulina, I.; et al. Chemical Engineering of Zeolites: Alleviating Transport Limitations through Hierarchical Design and Shaping. *Chem. Soc. Rev.* **2025**, *54*, 6335–6384. https://doi.org/10.1039/D5CS00169B.
49. Qian, R.; Zong, H.; Schneider, J.; et al. Charge Carrier Trapping, Recombination and Transfer during TiO_2 Photocatalysis: An Overview. *Catal. Today* **2019**, *335*, 78–90. https://doi.org/10.1016/j.cattod.2018.10.053.
50. Schneider, J.; Matsuoka, M.; Takeuchi, M.; et al. Understanding TiO_2 Photocatalysis: Mechanisms and Materials. *Chem. Rev.* **2014**, *114*, 9919–9986. https://doi.org/10.1021/cr5001892.
51. Zhang, L.; Mohamed, H.H.; Dillert, R.; et al. Kinetics and Mechanisms of Charge Transfer Processes in Photocatalytic Systems: A Review. *J. Photochem. Photobiol. C* **2012**, *13*, 263–276. https://doi.org/10.1016/j.jphotochemrev.2012.07.002.
52. Pavan, C.; Santalucia, R.; Escolano-Casado, G.; et al. Physico-Chemical Approaches to Investigate Surface Hydroxyls as Determinants of Molecular Initiating Events in Oxide Particle Toxicity. *Int. J. Mol. Sci.* **2023**, *24*, 11482. https://doi.org/10.3390/ijms241411482.
53. Kobayashi, T.; Ikeda, T.; Nakayama, A. Long-Range Proton and Hydroxide Ion Transfer Dynamics at the Water/CeO_2 Interface in the Nanosecond Regime: Reactive Molecular Dynamics Simulations and Kinetic Analysis. *Chem. Sci.* **2024**, *15*, 6816–6832. https://doi.org/10.1039/D4SC01422G.
54. Jeon, I.; Nam, K. Change in the Site Density and Surface Acidity of Clay Minerals by Acid or Alkali Spills and Its Effect on pH Buffering Capacity. *Sci. Rep.* **2019**, *9*, 9878. https://doi.org/10.1038/s41598-019-46175-y.
55. Chang, L.; Yong, S.-T.; Chai, S.-P.; et al. A Review of Methanol Photoreforming: Elucidating the Mechanisms, Photocatalysts and Recent Advancement Strategies. *Mater. Today Chem.* **2023**, *27*, 101334. https://doi.org/10.1016/j.mtchem.2022.101334.
56. Serna, C.; Ahlrichs, J.L.; Serratosa, J.M. Folding in Sepiolite Crystals. *Clays Clay Miner.* **1975**, *23*, 452–457. https://doi.org/10.1346/CCMN.1975.0230607.
57. Walczyk, A.; Karcz, R.; Kryściak-Czerwenka, J.; et al. Influence of Dry Milling on Phase Transformation of Sepiolite upon Alkali Activation: Implications for Textural, Catalytic and Sorptive Properties. *Materials* **2020**, *13*, 3936. https://doi.org/10.3390/ma13183936.
58. Prost, R. Infrared Study of the Interactions between the Different Kinds of Water Molecules Present in Sepiolite. *Spectrochim. Acta, Part A* **1975**, *31*, 1497–1499. https://doi.org/10.1016/0584-8539(75)80206-6.
59. Margenot, A.J.; Parikh, S.J.; Calderón, F.J. Fourier-Transform Infrared Spectroscopy for Soil Organic Matter Analysis. *Soil Sci. Soc. Am. J.* **2023**, *87*, 1503–1528. https://doi.org/10.1002/saj2.20583.
60. Gunasekaran, S.; Anbalagan, G.; Pandi, S. Raman and Infrared Spectra of Carbonates of Calcite Structure. *J. Raman Spectrosc.* **2006**, *37*, 892–899. https://doi.org/10.1002/jrs.1518.
61. Veerasingam, S.; Venkatachalapathy, R. Estimation of Carbonate Concentration and Characterization of Marine Sediments by Fourier Transform Infrared Spectroscopy. *Infrared Phys. Technol.* **2014**, *66*, 136–140. https://doi.org/10.1016/j.infrared.2014.06.005.
62. Yan, W.; Liu, D.; Tan, D.; et al. FTIR Spectroscopy Study of the Structure Changes of Palygorskite under Heating. *Spectrochim. Acta Part A* **2012**, *97*, 1052–1057. https://doi.org/10.1016/j.saa.2012.07.085.
63. Bourliva, A.; Sikalidis, A.K.; Papadopoulou, L.; et al. Removal of Cu^{2+} and Ni^{2+} Ions from Aqueous Solutions by Adsorption onto Natural Palygorskite and Vermiculite. *Clay Miner.* **2018**, *53*, 1–15. https://doi.org/10.1180/clm.2017.1.
64. Ichikawa, T.; Yamada, T.; Aoki, N.; et al. Surface Proton Hopping Conduction Mechanism Dominant Polymer Electrolytes Created by Self-Assembly of Bicontinuous Cubic Liquid Crystals. *Chem. Sci.* **2024**, *15*, 7034–7040. https://doi.org/10.1039/D4SC01211A.